Tissue stiffness mapping by light sheet elastography

Min Zhu[1,6], Kaiwen Zhang[1,2,6], Evan C. Thomas[1], Ran Xu[1,3], Brian Ciruna[1,3], Sevan Hopyan[1,3,4,*], Yu Sun[2,5,*]

1 Program in Developmental & Stem Cell Biology, Research Institute, The Hospital for Sick Children, Toronto, ON, M5G 0A4, Canada
2 Department of Mechanical and Industrial Engineering, University of Toronto, Toronto, ON, M5S 3G8, Canada
3 Department of Molecular Genetics, University of Toronto, Toronto, ON, M5S 1A8, Canada
4 Division of Orthopaedic Surgery, The Hospital for Sick Children and University of Toronto, Toronto, ON, M5G 1X8, Canada
5 Institute of Biomedical Engineering, University of Toronto, Toronto, ON, M5S 3G9, Canada
6 These authors contributed equally to this work

*Authors for correspondence:

Sevan Hopyan
686 Bay Street, 16-9713
Toronto, Ontario M5G 0A4
Canada
tel: 1 416 813 7654 X 301266
fax: 1 416 813 6414
sevan.hopyan@sickkids.ca

or

Yu Sun
5 King's College Road, MC419
Toronto, Ontario M5S 3G8
tel: 1 416 946 0549
fax: 1 416 978 7753
yu.sun@utoronto.ca

ABSTRACT
Tissue stiffness plays a crucial role in regulating morphogenesis, yet most existing measurement techniques cannot be applied *in vivo*. The few methods that do permit quantification of 3D tissue stiffness *in vivo* are invasive and offer low spatial and temporal resolution. Therefore, the dynamic progression of tissue stiffness cannot be monitored and mechanisms underlying how tissue stiffness regulates morphogenesis remain elusive. Here, we introduce light sheet elastography, a noninvasive method that couples low frequency shear waves with light sheet fluorescence microscopy. With this method, we achieved *in toto* stiffness mapping of organ-stage mouse and zebrafish embryos at cellular resolution. The versatility of the method enabled time-lapse stiffness mapping during tissue remodelling and of the beating embryonic heart. This method presents new opportunities for uncovering the dynamic regulation and consequences of tissue stiffness during morphogenesis.

INTRODUCTION
Morphogenesis involves complex coordination of biochemical and biophysical signals. Stiffness, a key mechanical property of tissue, plays a multifaceted role by modulating cell behaviours[1–3] and interacting with biochemical mediators[4–6]. A wholistic understanding of how this parameter contributes to development and may be manipulated to optimise tissue morphogenesis would require better measurement tools. The few state-of-the-art methods permitting *in vivo* measurement of 3D tissue stiffness require the injection of magnetic beads (magnetic tweezers)[3,7–9] or silica beads (optical tweezers)[10]. These methods are cumbersome, cause potential damage especially to sensitive tissues such as the developing brain and heart, and are limited in spatial resolution that relies on the positions of the deposited beads. Importantly, morphogenesis unfolds over time and invasive techniques fail to capture the temporal dynamics of stiffness, thereby limiting current studies to endpoint analyses. An ideal method would be noninvasive, permit high spatial and temporal resolution, and be sufficiently versatile for a substantial proportion of biologists using commercially available equipment.

Elastography is a noninvasive approach that consists of an actuation component to introduce local tissue deformation and an imaging tool to record the response of the tissue to quantify stiffness[11]. In terms of actuation principles, current elastography techniques can be categorised into optical and mechanical modes. Brillouin microscopy, based on the principle that the frequency shift of incident laser Brillouin scattering reflects stiffness, has been applied *in vivo*[12]. Although the acquisition speed and phototoxicity have been improved[13–15], a persistent limitation of Brillouin microscopy is that transparent tissues are required due to the method's reliance on known refractive indices, making it suboptimal for studying tissue stiffness in opaque organ-stage embryos. Moreover, the indirect relationship between Brillouin scattering in GHz and tissue elastic modulus in Pa potentially limits the quantitative utility of that approach[16]. In mechanically actuated elastography, the propagation speed of a shear wave is proportional to tissue stiffness. This approach has been applied clinically using ultrasound and magnetic resonance imaging for diagnosing stiffness-related diseases such as liver fibrosis[17]. Switching the imaging modality to optical microscopy has improved spatial resolution. However, a high actuation frequency in the kHz range has been required to enhance local phase contrast for

generating an observable phase shift to calculate shear wave propagation speed. This requirement arises from limited displacement tracking under brightfield imaging with particle imaging velocimetry[18]. Capturing sample response to such high-frequency actuation makes it incompatible with confocal or light sheet imaging and obviates 3D stiffness mapping. The high frequency actuation also leads to rapid amplitude attenuation, impeding whole embryo penetration.

To tackle these limitations, we developed a method for mapping stiffness by coupling mechanical actuation with light sheet fluorescence microscopy. A commercial piezoelectric device was used to propagate shear waves through organ-stage embryos (~ 3 mm). The shear wave displaced cells that were individually visualised by a far-red nuclear reporter H2B-miRFP703[19]. The robust far-red nuclear reporter offered high-contrast and deep-tissue imaging which, together with the use of a customised pattern-guide cell motion tracking program, enabled accurate reconstruction of local displacement patterns and distinguished phase shifts as low as 0.0023 rad at a low actuation frequency (≤10 Hz). We achieved whole embryo shear wave penetration and *in toto* tissue stiffness mapping at cellular (15 µm) resolution with time-lapse capability. Stiffness of the beating embryonic heart during ventricular contraction and relaxation was also mapped for the first time.

RESULTS

Light sheet elastography device

To optimise live imaging for mouse embryos, our device was built on a standard light sheet fluorescence microscope that provides high spatiotemporal resolution and minimises photobleaching. Simultaneous planar laser excitation and acquisition enabled by light sheet microscopy mitigates the confounding time delay caused by scanning (illuminating) the specimen by confocal microscopes. The light sheet elastography (LSE) device consists of a standard piezoelectric actuator (P-840.20, Physik Instrumente) that vibrates perpendicular to a capillary tube housing an agarose plug displaced up to ~30 µm. Piezoelectric actuation by a sinusoidal signal generates a shear wave through the agarose plug and the embryo embedded within it (Methods). The device also consists of a mounting stage secured to the microscope sample stage by permanent magnets (Figures 1A and 1B).

Dynamic phase analysis

Under ideal pure shear actuation as illustrated in Figure 1C and Movie S1, the local shear modulus *G* relates to local phase difference by[20]

$$G = \rho {c_s}^2 = \rho(\frac{2\pi f}{\Delta\varphi/\Delta y})^2$$

where ρ is density; c_s is shear wave propagation speed; f is actuation frequency; and $\Delta\varphi/\Delta y$ is the Y phase gradient. The establishment of the relationship was based on the principle that a forward-propagating wave passes specified point locations with a phase delay. For two points along the path of a shear wave that are in close proximity such that the material in between them can be considered homogeneous, the difference in the local phases at the two points is used to calculate the stiffness of the material between the two points. The local shear modulus *G* is related to elastic modulus *E* (a common metric for describing tissue stiffness) by

$$E = 2(1 + \upsilon)G$$

where υ is Poisson's ratio which is typically 0.5 for soft tissue[8].

In addition to the phase arising from pure shear wave propagation, other potential contributors to the phase of the extruded agarose gel are the phase inherited from the glass capillary above the gel, the damping effect of the culture medium, and the geometry (i.e., diameter and extrusion length) of the gel (Figure 1D and Supplementary Note).

To validate the phase-stiffness equation and evaluate the effect of potential contributing factors, we conducted shear wave actuation on 1% agarose gel that contained fluorescent beads. By tracking the displacement of the beads and fitting with the sinusoidal equation to decouple phase values (Methods), we obtained a local phase map of 1% agarose gel (Figure 1E). The phase map decays linearly along Y due to shear wave propagation with an average Y phase gradient of 51.8 rad/m. In addition to the Y phase, the phase also shows a linear symmetric decay along X with a ruffle fold that is inherited from the agarose gel inside the glass capillary (Figure 1G). The decay and ruffle fold resulted from wave propagation in the poroelastic material arising from the glass-gel boundary and wave interference, respectively[21] (Figure S1A and Supplementary Note). Inside the glass capillary, the agarose gel phase map exhibits the same X phase pattern as the extruded part without Y phase decay (Figures S1B-S1D). This X phase pattern was experimentally determined to be independent of Z location, glass capillary diameter, and agarose gel concentration (Figures S1E-S1G). The X phase speed (i.e., wave propagation speed) remained constant across different actuation frequencies, suggesting that the wave is non-dispersive (Figure S1H).

The extruded gel was found to be critically damped (i.e., damping ratio close to 1) by DMEM (Figure S2A and Supplementary Note). The critical damping effect filters out undesired wave reflection and mitigates its contribution to the local phase under forced oscillation[20]. DMEM damping arose from the added mass of the fluid that was displaced by the agarose gel and viscous fluid shear. From experimental and numerical simulation results, DMEM damping was dominated by mass damping (Figures S2B-S2F). Replacing the culture medium with fluids of different viscosities did not affect the phase result, as they all had a similar density to water. The critical damping effect extended to agarose gels of different elastic moduli and diameters (Figures S2G and S2H). We further verified that the rotational bending and deflection induced by the agarose gel's geometry was minimal and can be disregarded for phase analysis (Figures S2I-S2L and Supplementary Note). By performing actuation at different frequencies, Y phase speed was found to be constant (i.e., non-dispersive) as depicted in Figure S2M, indicating the predominantly elastic behavior of the agarose gel. The elastic behaviour of agarose gel was recapitulated by atomic force microscope (AFM) indentation (Figures S3A, S3B and Methods).

Hence, the phase in the extruded agarose gel is solved according to (see details in Supplementary Note)

$$\varphi = \varphi_x + \varphi_y = k_x \cdot |x| + k_s y = -2.25f|x| + \frac{\partial \varphi}{\partial y} y$$

where k_x and k_s are X and Y wavenumbers, respectively. Using our customised dynamic phase program (code link in Methods), the partial derivative of phase with respect to Y was computed, and the stiffness of 1% agarose gel was decoupled (Figure 1H) and determined to be 4.1 kPa on average. To validate LSE-measured stiffness, we compared the stiffness of 0.5% to 3% agarose gels quantified by LSE and by AFM indentation (Figure S3C). LSE measurements of agarose gel stiffness agreed well with AFM indentation results for concentrations ranging from 0.5% to 2% (i.e., <~10 kPa) within 7.45% difference. For agarose gels with concentrations above 2%, LSE measurements deviated from AFM indentation results by 20.94%. The discrepancy occurred because the frame rate of the Zeiss Z1 light sheet at 1000 × 1000 pixels was unable to capture the rapid propagation of shear waves to decouple the Y phase gradient in the stiff gel.

In toto tissue stiffness mapping

To achieve maximum tissue imaging penetration depth, we performed tissue stiffness mapping of an E9.25 mouse embryo using a transgenic far-red nuclear reporter H2B-miRFP703[19]. To track the fast moving, densely populated nuclei under shear wave propagation, we developed a motion tracking program utilising a subpixel image registration algorithm[22] (Figures S4A-S4D, S5A, Movie S2, and code link in Methods), capable of resolving a phase shift as small as 0.0023 rad. At E9.25, the mouse embryonic heart regularly beats at ~2 Hz (Figure 2A and Movie S3) with an amplitude that extends to ~200 µm away from the heart (Figure S5B). To compensate for the heartbeat, we chose our actuation frequency distinct from the beating frequency and eliminated the heartbeat signal using bandpass filtering (Figure S5A). The time resolution of LSE (i.e., number of frames required for a stable phase reading) was determined to be 7 frames (0.12 s) (Figure S5C). The spatial resolution was calculated as a function of the time resolution, actuation frequency, and sample stiffness considering a minimum signal-to-noise ratio of 3 (Methods). Within the stiffness range of most embryonic tissues (a few hundred Pa), neighbouring cells' phase difference can be resolved by LSE yielding cellular resolution (<15 µm) for stiffness mapping (Figures S5D, S5E, and Supplementary Note).

The stiffness of E9.25 mouse embryos was mapped by stitching sagittal plane tiles as shown in Figures 2B and 2C. The void areas in the stiffness map are cavities filled with intraembryonic fluid. Since shear waves do not propagate through fluid[23], cavities do not affect stiffness mapping results. The E9.25 embryo exhibited a stiff forebrain, hindbrain and somites with comparatively soft midbrain and optic vesicle regions. Similarly, we performed tissue stiffness mapping of a 16 hpf zebrafish embryo using the transgenic mScarlet nuclear reporter[24] (Methods). Individual tissues were then mapped and compared with published results. The LSE results agreed well with previously reported values for the E9.25 mouse forelimb bud, mandibular arch, and the 16 hpf zebrafish tail bud measured using AFM indentation[25,26] and magnetic tweezers[3,7,9] but with greater spatial detail (Figures 2B, 2C, S5F and S5G).

Time-lapse tissue stiffness mapping

The noninvasiveness of LSE also enabled time-lapse tissue stiffness mapping. We previously discovered an anteriorly biased tissue stiffness gradient in the mouse E9.25 forelimb bud by taking single time point measurements per embryo[3]. In contrast, LSE enabled time-lapse

stiffness mapping over a 3 h period. During that time, the stiffness gradient evolved such that the anterior bias expanded toward the central region (Figure 2F). That progression is consistent with an anterior to central transition of the distal peak of the limb bud as it expands between E9.25-E9.5[3,6].

The noninvasive nature of LSE also allows for stiffness mapping of mechanically sensitive tissues such as the beating embryonic heart, measurement of which cannot be achieved by existing methods. Experiments confirmed that 10 Hz LSE actuation for 1.7 seconds (i.e., 100 frames) did not induce any heartbeat frequency change or arrhythmia (Figure 3A). An important aspect of measuring heart stiffness is that shear wave propagation speed is affected by tissue stress[27]. To differentiate heart stiffness during ventricular relaxation and contraction, we first measured the time weighted average (>10 heartbeats) of E9.25 heart stiffness as shown in Figures 3B and 3C. The 0.12 s (i.e., 7 frames) time resolution allowed us to isolate stiffness during ventricular relaxation as shown in Figure 3D. Heart stiffness during ventricular contraction was decoupled according to

$$E_{heart} = \frac{E_{relax} \cdot t_{relax} \pm E_{contract} \cdot t_{contract}}{t_{relax} + t_{contract}}$$

and was 23.2% higher than in the relaxed state (Figures 3E and 3F). Whether the heartbeat increases or decreases the apparent stiffness depends on tissue stress which is determined by the superposition of contractile stress upon initial stress in the relaxed state. LSE can distinguish contributions of contractile stress to stiffness throughout the cardiac cycle.

DISCUSSION

This method of noninvasively mapping 3D tissue stiffness by LSE offers the potential for a panoramic view of tissue stiffness through various embryos and stages of development at a spatiotemporal resolution of 15 µm and 0.12 s. With a readily replicable setup, it is amenable for integration with a standard light sheet microscope. The noninvasive nature of this method also enables tissue stiffness mapping over time during development. LSE combined with live imaging of molecular reporters permits simultaneous visualisation of biomechanical and biochemical interactions *in vivo*, offering the potential to resolve ‘chicken-and-egg’ questions in morphogensis. Temporal progression of tissue stiffness also provides valuable inputs for computational modelling and simulation of morphogenetic events. In cardiac research, tissue stiffness has been somewhat a blind spot due to a lack of quantification tools. LSE’s ability to map stiffness throughout the cardiac cycle and during morphogenesis of various organ primordia opens avenues for proposing and testing hypotheses concerning development and congenital disease *in vivo* or *in vitro* using self-assembling organoids[28].

An opportune potential application is that LSE makes it possible to register single cell transcriptomic and proteomic datasets spatially with physical properties. Shear stress can activate signalling cascades and affects morphogenesis[29,30] and disease progression[31,32]. Therefore, aside from using LSE as a measurement tool, actuation with higher energy offers the potential to manipulate shear stress for testing mechanotransduction hypotheses.

REFERENCE

1. Mongera, A. *et al.* A fluid-to-solid jamming transition underlies vertebrate body axis elongation. *Nature* Preprint at https://doi.org/10.1038/s41586-018-0479-2 (2018).
2. Barriga, E. H., Franze, K., Charras, G. & Mayor, R. Tissue stiffening coordinates morphogenesis by triggering collective cell migration in vivo. *Nature* **554**, 523–527 (2018).
3. Zhu, M. *et al.* Spatial mapping of tissue properties in vivo reveals a 3D stiffness gradient in the mouse limb bud. *Proc Natl Acad Sci U S A* (2020) doi:10.1073/pnas.1912656117.
4. Hannezo, E. & Heisenberg, C. P. Mechanochemical Feedback Loops in Development and Disease. *Cell* **178**, 12–25 (2019).
5. Parada, C. *et al.* Mechanical feedback defines organizing centers to drive digit emergence. *Dev Cell* **57**, 854-866.e6 (2022).
6. Zhu, M. *et al.* Durotaxis bridges phase transition as a function of tissue stiffness in vivo. *bioRxiv* 2023.01.05.522913 (2023) doi:10.1101/2023.01.05.522913.
7. Serwane, F. *et al.* In vivo quantification of spatially varying mechanical properties in developing tissues. *Nat Methods* **14**, 181–186 (2017).
8. D'Angelo, A., Dierkes, K., Carolis, C., Salbreux, G. & Solon, J. In Vivo Force Application Reveals a Fast Tissue Softening and External Friction Increase during Early Embryogenesis. *Current Biology* (2019) doi:10.1016/j.cub.2019.04.010.
9. Zhu, M., Zhang, K., Tao, H., Hopyan, S. & Sun, Y. Magnetic Micromanipulation for In Vivo Measurement of Stiffness Heterogeneity and Anisotropy in the Mouse Mandibular Arch . *Research* (2020) doi:10.34133/2020/7914074.
10. Bambardekar, K., Clément, R., Blanc, O., Chardès, C. & Lenne, P.-F. Direct laser manipulation reveals the mechanics of cell contacts in vivo. *Proceedings of the National Academy of Sciences* (2015) doi:10.1073/pnas.1418732112.
11. Zhang, K., Zhu, M., Thomas, E., Hopyan, S. & Sun, Y. Existing and Potential Applications of Elastography for Measuring the Viscoelasticity of Biological Tissues In Vivo. *Front Phys* **9**, 670571 (2021).
12. Prevedel, R., Diz-Muñoz, A., Ruocco, G. & Antonacci, G. Brillouin microscopy: an emerging tool for mechanobiology. *Nature Methods 2019 16:10* **16**, 969–977 (2019).
13. Zhang, J., Nikolic, M., Tanner, K. & Scarcelli, G. Rapid biomechanical imaging at low irradiation level via dual line-scanning Brillouin microscopy. *Nature Methods 2023 20:5* **20**, 677–681 (2023).
14. Bevilacqua, C. *et al.* High-resolution line-scan Brillouin microscopy for live imaging of mechanical properties during embryo development. *Nature Methods 2023 20:5* **20**, 755–760 (2023).
15. Yang, F. *et al.* Pulsed stimulated Brillouin microscopy enables high-sensitivity mechanical imaging of live and fragile biological specimens. *Nature Methods 2023* 1–9 (2023) doi:10.1038/s41592-023-02054-z.
16. Raghunathan, R. *et al.* Evaluating biomechanical properties of murine embryos using Brillouin microscopy and optical coherence tomography. *https://doi.org/10.1117/1.JBO.22.8.086013* **22**, 086013 (2017).

17. Tang, A., Cloutier, G., Szeverenyi, N. M. & Sirlin, C. B. Ultrasound elastography and MR elastography for assessing liver fibrosis: Part 1, principles and techniques. *American Journal of Roentgenology* **205**, 22–32 (2015).
18. Grasland-Mongrain, P. *et al.* Ultrafast imaging of cell elasticity with optical microelastography. *Proc Natl Acad Sci U S A* **115**, (2018).
19. Gu, B., Posfai, E. & Rossant, J. Efficient generation of targeted large insertions by microinjection into two-cell-stage mouse embryos. *Nat Biotechnol* (2018) doi:10.1038/nbt.4166.
20. Yoshida, S. Waves: Fundamentals and dynamics. *Waves: Fundamentals and dynamics* (2017) doi:10.1088/978-1-6817-4573-2.
21. Walker, J. M. *et al.* Nondestructive evaluation of hydrogel mechanical properties using ultrasound. *Ann Biomed Eng* **39**, 2521–2530 (2011).
22. Thurman, S. T., Guizar-Sicairos, M. & Fienup, J. R. Efficient subpixel image registration algorithms. *Optics Letters, Vol. 33, Issue 2, pp. 156-158* **33**, 156–158 (2008).
23. Taljanovic, M. S. *et al.* Shear-Wave Elastography: Basic Physics and Musculoskeletal Applications. *https://doi.org/10.1148/rg.2017160116* **37**, 855–870 (2017).
24. Burgess, J. *et al.* An optimized QF-binary expression system for use in zebrafish. *Dev Biol* **465**, 144–156 (2020).
25. Tao, H. *et al.* Oscillatory cortical forces promote three dimensional cell intercalations that shape the murine mandibular arch. *Nat Commun* (2019) doi:10.1038/s41467-019-09540-z.
26. Lau, K. *et al.* Anisotropic stress orients remodelling of mammalian limb bud ectoderm. *Nat Cell Biol* **17**, 569–579 (2015).
27. Martin, J. A., Schmitz, D. G., Ehlers, A. C., Allen, M. S. & Thelen, D. G. Calibration of the shear wave speed-stress relationship in ex vivo tendons. *J Biomech* **90**, 9–15 (2019).
28. Lewis-Israeli, Y. R. *et al.* Self-assembling human heart organoids for the modeling of cardiac development and congenital heart disease. *Nature Communications 2021 12:1* **12**, 1–16 (2021).
29. Steed, E. *et al.* klf2a couples mechanotransduction and zebrafish valve morphogenesis through fibronectin synthesis. *Nature Communications 2016 7:1* **7**, 1–14 (2016).
30. Kale, G. R. *et al.* Distinct contributions of tensile and shear stress on E-cadherin levels during morphogenesis. *Nature Communications 2018 9:1* **9**, 1–16 (2018).
31. Baeyens, N., Bandyopadhyay, C., Coon, B. G., Yun, S. & Schwartz, M. A. Endothelial fluid shear stress sensing in vascular health and disease. *J Clin Invest* **126**, 821–828 (2016).
32. Lee, H. J. *et al.* Fluid shear stress activates YAP1 to promote cancer cell motility. *Nature Communications 2017 8:1* **8**, 1–14 (2017).
33. Ahmad, A. *et al.* Magnetomotive optical coherence elastography using magnetic particles to induce mechanical waves. *Biomedical Optics Express, Vol. 5, Issue 7, pp. 2349-2361* **5**, 2349–2361 (2014).
34. Sader, J. E. Frequency response of cantilever beams immersed in viscous fluids with applications to the atomic force microscope. *J Appl Phys* **84**, 64–76 (1998).
35. Thomson, W. Tyrrell. & Dahleh, M. Dillon. Theory of vibrations with applications. 524 (2014).

36. Cowper, G. R. The Shear Coefficient in Timoshenko's Beam Theory. *J Appl Mech* **33**, 335–340 (1966).
37. Giurgiutiu, V. Structural health monitoring with piezoelectric wafer active sensors. *16th International Conference on Adaptive Structures and Technologies* 94–100 (2006) doi:10.1016/C2013-0-00155-7.
38. Auld, B. A. (1922-). Acoustic fields and waves in solids. Vol. 2. (1990).
39. Repetto, C. E., Roatta, A. & Welti, R. J. Forced vibrations of a cantilever beam. *Eur J Phys* **33**, 1187 (2012).

MATERIALS AND METHODS

Animal strains

Analysis was performed using the mouse strain: R26-CAG-H2B-miRFP703 [The Jackson Laboratory: Gt(ROSA)26Sor$^{em1.1(CAG-RFP*)Jrt}$/J],outbred to CD1; and the zebrafish strain Tg(ubi:loxp:mScarlet-nls:loxp:QFGal4)[24], outbred to TU. All animal experiments were performed in accordance with Canadian Council on Animal Care (CCAC) guidelines, and protocols approved by the Hospital for Sick Children Research Institute Animal Care Committee.

Light sheet elastography device

The piezoelectric actuator used in this work is P-840.20 (Physik Instrumente). It was attached to the light sheet microscope (Zeiss Lightsheet Z.1) via a mounting stage that was 3D printed using acrylonitrile butadiene styrene (ABS). Three permanent magnets (McMASTER-CARR Lot 5862k178) were used to secure the mounting stage to the Z.1 motorised sample stage. The glass capillary and plunger are standard components for the Z.1. Customised glass capillary holders were 3D printed from resin to connect the glass capillary and actuator. A simple sinusoidal waveform, generated by a function generator (B&K Precision Lot 4053B) and amplified by a custom-made voltage amplifier, was used to drive the piezoelectric actuator. The custom-made voltage amplifier provides a maximum voltage output of 100 V, enabling a travel range of up to 30 μm for the piezoelectric actuator. The design files of the mounting stage, glass capillary holder and voltage amplifier are available for download at https://github.com/MinZhuUOTSickKids/light_sheet_elastography.

Agarose gel validation

To validate light sheet elastography, we performed stiffness mapping of 0.5 to 3% low melting point agarose gel (ThermoFisher Lot 16520050) in DMEM without phenol red and compared the results to those obtained with AFM indentation. The agarose gel solution contained 5% fluorescent beads (1:200; Sigma Lot L3030). Once the agarose solidified, the glass capillary was submerged into the imaging chamber containing DMEM without phenol red, and the agarose plug was partially extruded from the glass capillary. The temperature of the imaging chamber was maintained at 37°C with 5% CO_2. Upon actuation, the displacements of the fluorescent beads were tracked using Imaris (Bitplane) and fitted in MATLAB (MathWorks) to obtain the phase map. The stiffness map of the agarose gel was resolved from the phase map by computing the phase decay along Y axis.

The stiffness of the same batch agarose gel was also evaluated by AFM (Bruker BioScope Catalyst) mounted on an inverted microscope (Nikon Eclipse-Ti) at 37°C with 5% CO_2. A spherical probe tip with a diameter of 32 μm was used for all indentations performed. The spherical tip was made by assembling a borosilicate glass microsphere onto a tipless AFM cantilever using epoxy glue. After assembly, the diameter of the probe tip was measured under a scanning electron microscope (Hitachi 4000). The spring constant of the cantilever was calibrated by measuring the power spectral density of the unloaded cantilever thermal noise fluctuation. The approach-retraction curve of each indentation was fitted with the Hertz model for a spherical tip to obtain stiffness.

Time-lapse tissue stiffness mapping

Dissected embryos were suspended in a solution of DMEM without phenol red containing 12.5% filtered rat serum, 1% low-melt agarose (Invitrogen), and 1% fluorescent beads (1:500, Sigma Lot L3030) that were used for drift-compensation within a glass capillary. Once the agarose solidified, the capillary was submerged into an imaging chamber containing DMEM without phenol red, and the agarose plug was partially extruded from the glass capillary tube until the portion containing the embryo was completely outside of the tube. The temperature of the imaging chamber was maintained at 37°C with 5% CO_2. Images were acquired for 3 to 4 h at 5 min. intervals.

Pattern-guided cell motion tracking program

The tracking function in Imaris (Bitplane) is not applicable to the densely populated and fast-moving cells in the LSE embryo dataset as shown in Movie S2. Based on Python, we developed a pattern-guided cell motion tracking program for tracking these cells, utilising a subpixel image registration algorithm[22]. The algorithm compares two images and computes the pixel translation between them by maximising intensity correlation with respect to translation in the two directions. The 0.0029 pixels motion tracking resolution permits resolving phase shifts as small as 0.0023 rad. With a user interface, our program allows the selection of a working area to track the average motion. It then tracks selected points within the working area by comparing small areas around each point over time. The points themselves and size of the areas around the points to be tracked are user selectable. The output is the positions of the selected points at each time point. The program is available for download at https://github.com/MinZhuUOTSickKids/light_sheet_elastography.

Spatiotemporal resolution of LSE

The time resolution was determined by fitting varying numbers of frames to the sinusoidal function $A\ cos\ (\omega t + \varphi)$. We fitted 3 to 100 frames at an interval of 1 frame. The phase reading was found to stabilize after 7 frames (Figure S5B). To evaluate the spatial resolution of LSE, we quantified the phase root mean squared (RMS) level as a measure of noise, as shown in Figure S5D. The phase RMS is inversely related to time resolution by a power law relation. Considering a signal-to-noise ratio of 3, the minimum phase shift that can be differentiated by LSE is

$$\Delta\varphi = 3\varphi_{RMS} = 0.07425{t_{reso}}^{-0.7597}$$

By rewriting the shear modulus - phase shift equation

$$\frac{\Delta\varphi}{\Delta y} = 2\pi f\sqrt{\frac{\rho}{G}} = 2\pi f\sqrt{\frac{2(1+\upsilon)\rho}{E}}$$

and substituting values in the equation, the spatial resolution of LSE (Δy) in microns is

$$s_{reso} = \Delta y = \frac{215.75\sqrt{E}}{f \cdot {t_{reso}}^{0.7597}}$$

Thus, the spatial resolution at 10 Hz actuation is shown in Figure S5E.

Data Availability

The data that support the findings of this study are available at https://figshare.com/articles/dataset/light_sheet_elastography.

Code Availability

All custom codes used in this paper are available at https://github.com/MinZhuUOTSickKids/light_sheet_elastography.

ACKNOWLEDGEMENTS

We thank Teng Cui for help with mechanics analysis, and Sepehr Saber for help with DMEM viscosity measurement. This work was funded by the Canada First Research Excellence Fund/Medicine by Design (MbDGQ-2021-04 to SH/YS and MPDF-2020-04 to MZ, and the Canadian Institutes of Health Research (168992) to SH/YS. YS also acknowledges support from the Canada Research Chairs program.

AUTHOR CONTRIBUTIONS

M.Z. and K.Z. designed and performed the experiments, modelling, and wrote the manuscript; E.T. wrote the tracking program. R.X and B.C. provided zebrafish experimental support. M.Z., Y.S. and S.H. co-conceived the project. Y.S. and S.H. co-funded the project and edited the manuscript.

SUPPLEMENTARY MOVIE LEGENDS

Movie S1

Animation illustrating LSE under ideal pure shear actuation.

Movie S2

LSE cell tracking results using Imaris versus our new tracking tool, pattern-guided cell motion tracking (PCMT).

Movie S3

LSE actuation on an E9.25 H2B-miRFP703 embryonic heart.

SUPPLEMENTARY NOTE

Analysis of shear wave propagation in agarose gel

A prerequisite for using shear wave propagation to quantify stiffness was to establish a phase-shear wave propagation speed relation. The complexity of the multi-physical interactions within the system affirmed the impracticality of an analytical approach. Therefore, we strategised our analysis by identifying and examining the contributing factors of the local phase to arrive at an empirical solution for local phase. For this purpose, we discuss: 1) general wave equation, 2) material behaviour under actuation, 3) baseline phase pattern, 4) propagation of longitudinal waves, 5) propagation of shear waves, 6) culture medium damping, and 7) geometry considerations. A summary of these contributing factors was illustrated in Figure 1D.

1. General wave equation

For a one-dimensional system under the influence of propagating waves along X induced by an external force, the general form of the one-dimensional wave equation is[20]

$$\frac{\partial^2 U}{\partial t^2} + \eta \frac{\partial U}{\partial t} = c^2 \frac{\partial^2 U}{\partial x^2} + \frac{F(t)}{m}$$

where c is the wave propagation speed, and damping coefficient is denoted as η. For waves propagating in the absence of damping, the above equation simplifies to

$$\frac{\partial^2 U}{\partial t^2} = c^2 \frac{\partial^2 U}{\partial x^2} + \frac{F(t)}{m}$$

The general solution is,

$$U(x,t) = A_x e^{i\phi} = A_x e^{i(\pm\varphi \pm \omega t)} = A_x e^{i(\pm kx \pm \omega t)}$$

where ϕ is phase angle, φ is local phase due to wave propagation, and k is wavenumber.

2. Material behaviour under actuation

Characteristics of the excitation signal underpin the baseline behaviour of the system. Since the piezoelectric actuator was driven by a sinusoidal signal, the displacement function, $U_0(t)$, takes on the form,

$$U_0(t) = A_0 \cos 2\pi f t = A_0 \cos \omega t$$

where A_0 is the amplitude of the signal, f is the temporal actuation frequency, and ω is the angular actuation frequency. To achieve optimal tracking and curve fitting results, it is important to maintain an adequate amplitude while avoiding excessive rotational bending and deflection (refer to the geometry considerations section). We conducted an experimental parametric sweep of the amplitude from 5-15 μm with a step size of 1 μm. An amplitude above 10 μm provided a good fit, and in the 10-15 μm range, the R-squared value was above 0.98. The actuation frequency was selected based on the microscope settings and viscoelastic behavior of agarose gel. In a typical 1000 × 1000 pixels setting, the Zeiss Lightsheet Z.1 gives a frame rate of 57.2 Hz limiting the maximum actuation frequency to 28.6 Hz according to the Nyquist-Shannon sampling theorem. To mitigate the viscoelastic behaviour of the agarose gel for a simple solution of phase, an actuation frequency sweep from 5 to 25 Hz with an amplitude of 15 μm was conducted. We found that actuation frequencies under 10 Hz yield good tracking results, with the phase speed being independent of frequency in both the X and Y axes, suggesting elastic behaviour (Figures S1H and S2M). From the AFM indentation experiment performed under same strain rate estimated by simulation, no indent-retract hysteresis was

observed, which further validated the predominant elastic behaviour of agarose gel as shown in Figure S3B.

When a structure undergoes forced oscillation, the actuation induces a collection of local interactions among the particles within the structure. The local displacement pattern is determined by direct actuation and other system-specific factors. At steady state, the generalised displacement of each particle located at (x, y) takes the following form[20],

$$U_{x,y}(x, y, t) = A_{x,y}\ cos\ (\omega t + \varphi_{x,y}\ )$$

where $\varphi_{x,y}$ is the local phase. The phase of the extruded agarose gel consists of two parts: the shear wave propagation phase along the Y-axis and the phase inherited from the agarose gel inside the glass capillary, henceforth referred to as the baseline phase.

3. Baseline phase pattern

To establish a baseline phase pattern, we conducted sinusoidal actuation and tracked the displacement of fluorescent beads embedded in the agarose gel. The field-of-view used was 2.6 mm × 2.6 mm covering the entire agarose gel within the glass capillary. The displacement of an individual bead was tracked by weighted pixel intensity and fitted with a sinusoidal function to obtain the local phase $\varphi_{x,y}$. For each actuation, over 300 fluorescent beads were tracked and fitted with R-squared values above 0.98 to generate the baseline phase pattern as shown in Figure S1B. The baseline phase pattern displayed a symmetrical decay along X folded at the center of the capillary without changes in phase along Y (Figures S1C and S1D). Multiple ruffle folds were located along X at a phase interval of ~0.075 rad. The X phase gradient was independent of Z location, glass capillary diameter, and stiffness (i.e., agarose gel concentration) as shown in Figures S1E-S1G. The X phase speed (i.e., wave propagation speed) was found to be constant at different actuation frequencies suggesting the wave being non-dispersive. The X phase pattern results from a complex interplay of boundary conditions, including adhesion and decohesion between the gel and glass capillary, as well as wave propagation, reflection, and interference.

4. Longitudinal wave propagation

Longitudinal wave propagation contributes to displacement along the X axis inside the glass capillary. Based on the general wave equation, the displacement due to longitudinal wave propagation without viscous damping effect can be expressed as,

$$U_x(x, t) = A_x e^{i\phi} = A_x e^{i(\pm\varphi_l \pm \omega t)} = A_x e^{i(\pm k_l x \pm \omega t)}$$

where ϕ is the phase angle, φ_l is the local phase due to longitudinal wave propagation, and k_l is the longitudinal wavenumber. If only the real-time forward-moving longitudinal wave is considered, the horizontal displacement pattern of a particle at X can be expressed as,

$$U_x(x, t) = A_x\ cos\ \ (k_l y - \omega t)$$

The local phase due to longitudinal wave propagation φ_l is a function of the horizontal location of the particles, i.e.,

$$\varphi_l = k_l x$$

The longitudinal wavenumber k_l can be used to calculate the propagation speed of the longitudinal wave c_l, which is determined by the longitudinal modulus M and density ρ of the material by,

$$k_l = \frac{\omega}{c_l} = \frac{\omega}{\sqrt{\frac{M}{\rho}}}$$

Longitudinal wave propagates at a speed around 1,500 m/s in agarose gels of different concentrations[21] which corresponds to a phase gradient along X axis, $\Delta\varphi_l/\Delta x = 0.0016$ rad/mm (less than 1% of the observed X phase gradient in the capillary) under 10 Hz actuation. The phase delay caused by longitudinal wave propagation can therefore be neglected from our phase analysis. The longitudinal wave propagation speed in agarose gel was discovered to be dominated by the fluid component which constitutes over 90% of its mass and largely independent of gel stiffness (i.e., concentrations)[21]. Considering the insufficient imaging frame rate offered by Zeiss Z.1 (i.e., up to 100 fps) to capture the rapid propagation, decoupling the longitudinal modulus of the gel from its propagation speed is infeasible.

5. Shear wave propagation

In the extruded gel, the horizontal motion of particles located along Y at a fixed X can be perceived as a 1D system under the influence of Y-propagating shear waves. Based on the general wave equation, the displacement due to shear wave propagation without damping effect can be expressed as,

$$U_y(y,t) = A_y e^{i\phi} = A_y e^{i(\pm\varphi_s \pm \omega t)} = A_y e^{i(\pm k_s x \pm \omega t)}$$

where ϕ is the phase angle, φ_s is the local phase due to shear wave propagation, and k_s is the shear wavenumber. If only the real-time forward-moving shear wave is considered, the horizontal displacement pattern of a particle at Y can be expressed as,

$$U_y(y,t) = A_y \cos\ (k_s y - \omega t)$$

The local phase due to shear wave propagation φ_s is a function of the vertical location of the particles, i.e.,

$$\varphi_s = k_s y$$

The shear wavenumber (k_s) can be used to quantify the shear modulus (G) of the material via,

$$k_s = \frac{\omega}{c_s} = \frac{\omega}{\sqrt{\frac{G}{\rho}}}$$

Unlike longitudinal waves, shear waves propagate at a much lower speed in agarose gels (a few m/s)[33], making it ideal for decouple the shear modulus of the gel.

6. Culture medium damping

The medium in which the gel was submerged, DMEM, served multiple purposes. First, DMEM acted as a culture medium that supported the viability and growth of a living biological sample. Second, DMEM has a similar density to agarose gel, thus counterbalancing the effect of gravity loading on the actuated gel through buoyancy. DMEM also served as an external damping source to minimize wave reflections and gel rotational bending and deflection induced by the actuation. DMEM damping can be separated into two parts, the added mass of the fluid that is displaced by the agarose gel (i.e., mass damping) and the viscous fluid shear at the surface of the gel (viscous damping).

To investigate the effect of DMEM damping on local phase, we considered DMEM as an infinite medium since the size of the chamber is orders of magnitudes larger than the actuation amplitude. Based on the general wave equation, $\eta \frac{\partial U}{\partial t}$, was introduced. The solution for a damped wave acquired a complex form ($\widetilde{U}$) that can be expressed as follows[20],

$$\widetilde{U}_x(x,t) = A_x e^{i(\tilde{k}x-\omega t)} = A_x e^{i((Re(\tilde{k})+Im(\tilde{k}))x-\omega t)} = A_x e^{iIm(\tilde{k})x} e^{i(Re(\tilde{k})x-\omega t)}$$

The real term of the solution became,

$$U_x(x,t) = A_x e^{iIm(\tilde{k})x} cos\,(Re(\tilde{k})x - \omega t)$$

The complex wavenumber $\tilde{k}$ consisted of a real part, $Re(\tilde{k})$, and an imaginary part, $Im(\tilde{k})$, whose expressions take the following forms,

$$Re(\tilde{k}) = \frac{\omega}{\sqrt{2}c}\left(\sqrt{1+\left(\frac{\eta}{\omega}\right)^2}+1\right)^{\frac{1}{2}}$$

$$Im(\tilde{k}) = \frac{\omega}{\sqrt{2}c}\left(\sqrt{1+\left(\frac{\eta}{\omega}\right)^2}-1\right)^{\frac{1}{2}}$$

As a result, adding a damping component affects both local amplitude and phase. The magnitude to which their values are altered depends on the damping coefficient η. The damping ratio ζ relates η and undamped natural frequency of the system ω_n by,

$$\zeta = \frac{\eta}{2\omega_n}$$

The damping ratio ζ can vary from undamped ($\zeta=0$), underdamped ($\zeta<1$), critically damped ($\zeta=1$) to overdamped ($\zeta>1$). Experimental observations indicated that our system was closely approaching critical damping by DMEM as illustrated in Figure S2A. To investigate the impact of system parameters (e.g., gel extrusion length) on the damping behavior and the source of DMEM-induced damping (i.e., mass vs. viscous damping), we conducted COMSOL fluid-structure interaction (FSI) simulations. The inputs of the simulation are illustrated in Figure S2D. DMEM was modelled as linearized Navier-Stokes with a dynamic viscosity of 1.3 mPa·s measured using a rheometer (TA Instruments, AR 2000) at 37 °C. The input elastic modulus for 1% agarose was 4.05 kPa determined by AFM indentation at 37 °C. We simulated 1% agarose gel with an extrusion length ranging from 3-18 mm, given the fact that 3 mm being the minimum length required to properly fit an E9.25 mouse embryo whereas 18 mm being the maximum length without interfering with the imaging chamber. For extrusion lengths less than 12 mm, the damping ratio clustered around 1, suggesting a critical damping state. As the extrusion exceeded 12 mm, the damping ratio continued to decrease, moving the system into an underdamped state. By sweeping the culture medium viscosity (from 0.5 to 1.5 mPa·s) and density (0.5 to 1.5 g/cm^3) in the FSI simulation, we found that damping ratio is predominantly determined by density (Figure S2F). Since various culture media have densities similar to that of water, replacing the culture medium with different viscosity in the LSE experiment does not affect the critical damping conclusion. This was experimentally validated by substituting DMEM with water (viscosity: 0.69 mPa·s at 37 °C), as depicted in Figures S2B and S2C. By sweeping through agarose gel elastic moduli (0.5% to 3%, as determined by AFM) and four stock Zeiss Z.1 glass capillaries of different inner diameters, critical damping effect was verified for different gel percentage and diameter (Figures S2G and S2H).

In summary, for agarose gel with an extrusion length spanning from 3 to 12 mm, the system can be regarded as being critically damped. The critical damping effect, dominated by the density of culture medium, filters out undesired wave reflection and mitigates its contribution to the local

phase under forced oscillation[20]. As a result, the damping effect can be disregarded for phase analysis. It is noted that, as the dimensions of the agarose gel (diameter and extrusion length) decrease to the micrometer level (e.g., AFM cantilever), the influence of viscous damping becomes significant and must be taken into consideration[34].

7. Geometric considerations

For the analysis of shear wave propagation, agarose gel was simplified as a one-dimensional system. The loaded three-dimensional structure of agarose gel imposes rotational bending and deflection governed by beam vibration theories. Understanding the particle's response to local rotational bending and deflection is necessary for the phase evaluation as well as the design of the post-processing algorithm. Under a dynamic load, $F(t)$, the characteristics of a homogenous, isotropic, linearly elastic thin beam with a uniform transverse cross-section XZ under a small deformation can be described by Timoshenko-Ehrenfest beam theory (TEBT). The horizontal displacement pattern U is[35],

$$EI\frac{\partial^4 U}{\partial y^4} + m\frac{\partial^2 U}{\partial t^2} - \left(\rho I + \frac{mEI}{\kappa SG}\right)\frac{\partial^4 U}{\partial y^2 \partial t^2} + \frac{m\rho I}{\kappa SG}\frac{\partial^4 U}{\partial t^4} = F + \frac{\rho I}{\kappa SG}\frac{\partial^2 F}{\partial t^2} - \frac{EI}{\kappa SG}\frac{\partial^2 F}{\partial y^2}$$

with I representing the second moment of area of the structure, m representing the mass of the structure, S representing the transverse cross-sectional area, and κ representing the Timoshenko shear coefficient that depends on the cross-sectional geometry. For a solid beam with a circular transverse cross-section, κ is 0.9[36]. The dynamic load introduced a rigid movement, with the time-dependent terms representing a combined effect of inertia and shear forces concerning local rotation as a function of Y, and the fourth-order partial derivative with respect to Y characterizing local deflection. Considering the minimal damping effect from DMEM and no sliding motion between the gel and glass capillary, our system can be modelled as a free-end at $y = L$ and a fix-end at $y = 0$.

A low actuation frequency results in an actuation wavelength longer than the length of the extruded gel. For 1% agarose gel under 10 Hz actuation, the actuation wavelength was 1.16 m while the extrusion length of the gel was less than 12 mm. The system resembles a beam undergoing first-mode antisymmetric flexural vibration[37]. The portion to one side of the central axis ($x = 0$) would be under tension while the other side be under compression at an arbitrary time point and vice versa. The macroscopic distortion of the geometry can be decomposed into local rotation at the single-particle level. To study the characteristics of local rotation, the Timoshenko beam equation is rewritten in its equivalent coupling form by directly integrating the angle of rotation,

$$\rho S\frac{\partial^2 U}{\partial t^2} - kSG\frac{\partial^2 U}{\partial y^2} + kSG\frac{\partial \theta}{\partial y} = F$$

$$\rho I\frac{\partial^2 \theta}{\partial t^2} - EI\frac{\partial^2 \theta}{\partial y^2} - kSG\frac{\partial U}{\partial y} + kSG\theta = 0$$

The rotational effect can be understood through the angle of rotation, θ, as a function of the particle location along y. For a particle located at y, the 2D displacement field vector D is composed of the horizontal U and vertical displacement V vectors by[38],

$$D = U + V$$

The angle of rotation is defined as,

$$\theta = \frac{|V|}{|U|}$$

The local rotation induces an elliptically polarized motion instead of a pure horizontal motion (X direction) as shown in Figure S2I. We next examined the local rotation along the X and Y axes. Along the X axis, minimum rotation was observed near the central axis. A linear relation was found between the horizontal distance from the central axis and angel of rotation (Figure S2J). Along the Y axis, the maximum angle of rotation at boundary increased with Y location but plateaued at 0.15 rad as shown in Figure S2K. Therefore, the displacement of particles was approximated as U.

For local deflection, the inertial and shearing effects can be excluded, resulting in a simplified form of TEBT known as the Euler-Bernoulli beam theory (EBBT) that can be expressed as [39],

$$EI\frac{\partial^4 U}{\partial y^4} + \rho S\frac{\partial^2 U}{\partial t^2} = 0$$

Premised on the given boundary conditions, the fix-end adopts the displacement function, $U_0(t)$, as prescribed by the piezoelectric actuator with no Y dependence. The free-end is assumed to be without rotational or shearing forces. The boundary conditions can be expressed as,

$$U(0,t) = A_0\, cos\, \omega t\, , \frac{\partial U(0,t)}{\partial y} = 0$$

$$\frac{\partial^2 U(L,t)}{\partial y^2} = 0, \frac{\partial^3 U(L,t)}{\partial y^3} = 0$$

The solution is,

$$U(y,t) = (a_1 cosh\,(\beta y)\ + a_2 sinh\,(\beta y)\ + (A_0 - a_1) cos\,(\beta y)\ - a_2 sin\,(\beta y)\,)\, U_0(t)$$

with the coefficients as,

$$\beta = \left(\frac{\rho S\omega^2}{EI}\right)^{\frac{1}{4}}$$

$$a_1 = A_0 \frac{cosh\,\beta L\ \ cos\,\beta L + sinh\,\beta L\ \ sin\,\beta L\ + 1}{2(1 + cosh\,\beta L\ \ cos\,\beta L\,)}$$

$$a_2 = -A_0 \frac{cosh\,\beta L\ \ sin\,\beta L + sinh\,\beta L\ \ cos\,\beta L}{2(1 + cosh\,\beta L\ \ cos\,\beta L\,)}$$

The solution of EBBT suggests an increase in the displacement amplitude towards +Y which was confirmed by experimental results (Figure S2L). The increase in displacement amplitude does not affect the local phase since U and U_0 remain in phase when located away from the node. The increased local bead movement speed induced by the increased displacement amplitude undermines tracking accuracy. As such, to achieve optimal tracking results, we limited the maximum actuation frequency to 10 Hz.

Conclusion

During light sheet live imaging, considering that longer gel extrusion length can cause tissue drift over time, we selected extrusion length from 6 to 7 mm for our tissue stiffness mapping experiments with a maximum actuation frequency of 10 Hz for optimal tracking results. As analysed in previous sections, the phase relationship can be empirically solved as,

$$\varphi = \varphi_x + \varphi_y = k_x \cdot |x| + k_s y = -2.25 f|x| + \frac{\partial \varphi}{\partial y} y$$

where k_x and is k_s are X and Y wavenumbers, respectively.

Figure 1

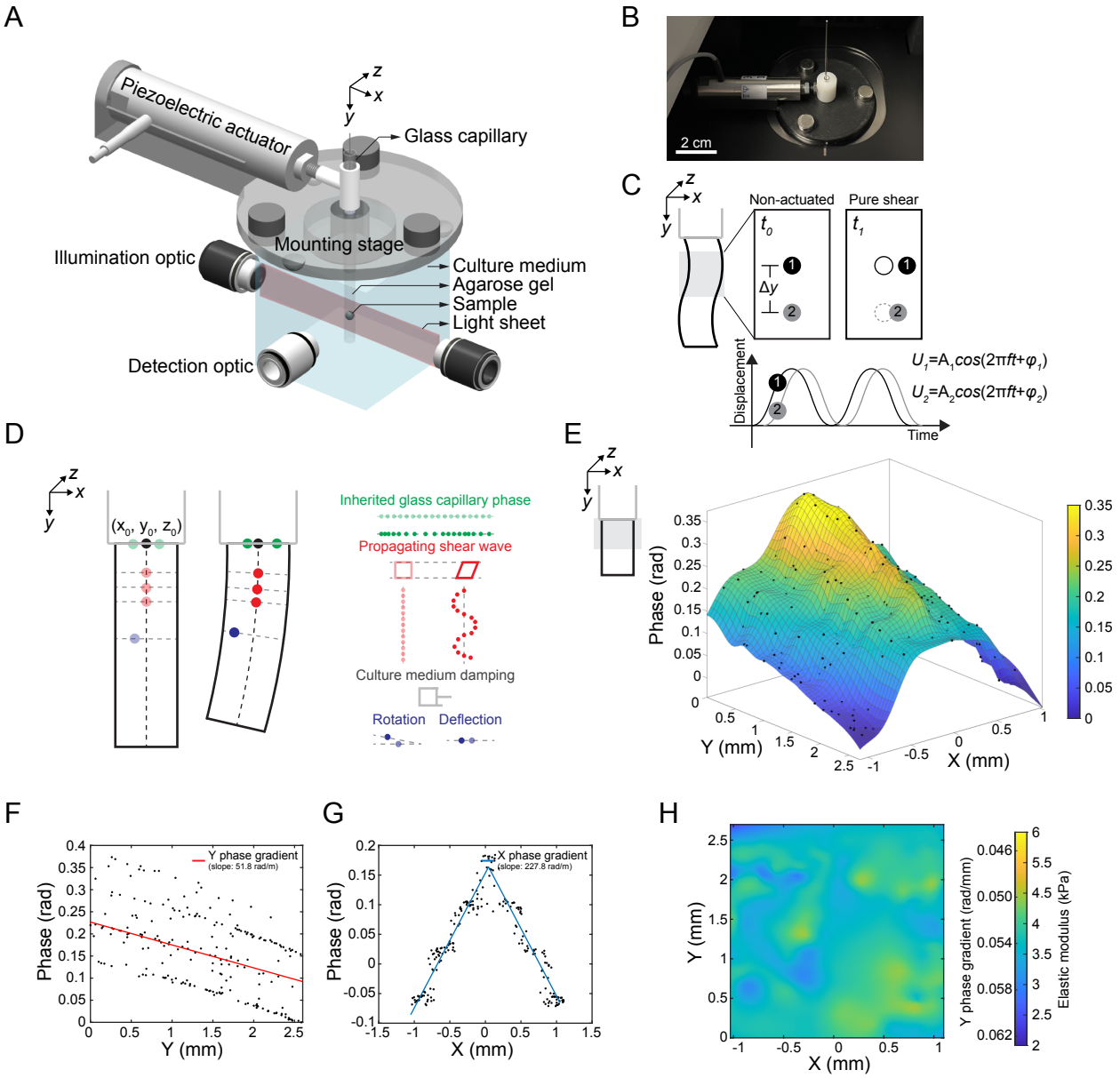

Light sheet elastography. (A) 3D structure of the LSE device. (B) Experimental setup of LSE. (C) Schematic illustrating ideal pure shear wave propagation causing a phase delay along Y axis. (D) Schematic describing potential contributors to the local phase. (E) 3D rendered phase map of 1% agarose gel under 10 Hz actuation. (F) YZ projection of the phase map shown in E showing linear phase decay induced by shear wave propagation along Y axis. (G) Inherited glass capillary phase along X axis. (H) Stiffness map of 1% agarose gel. Colour-coded scale showing elastic modulus and its corresponding Y phase gradient under 10 Hz actuation.

Figure 2

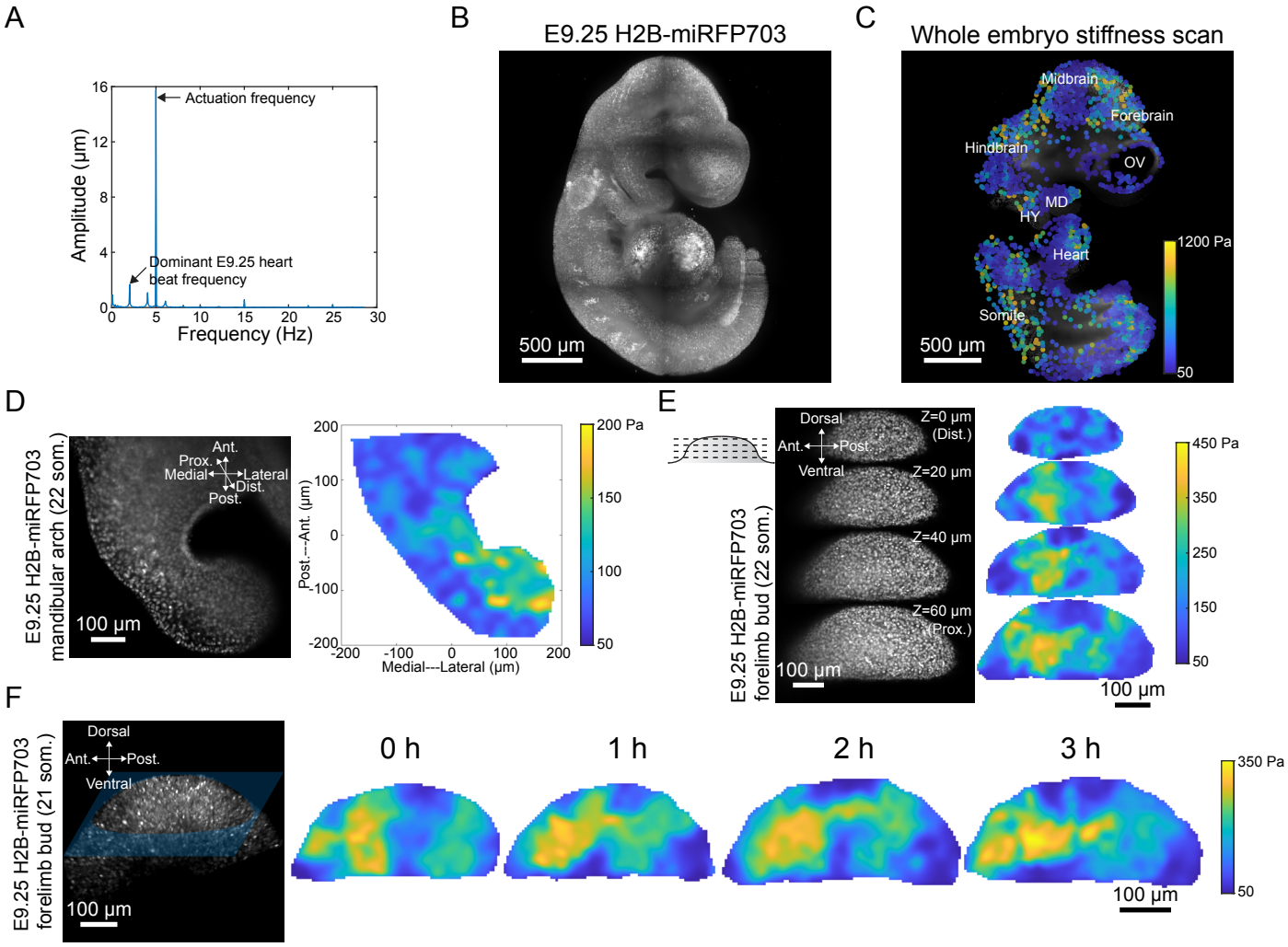

Non-invasive tissue stiffness mapping. (A) Fast Fourier transform of a heart cell under 5 Hz actuation. (B) 3D rendering of an E9.25 H2B-miRFP703 mouse embryo. (C) Slice view of a E9.25 whole embryo stiffness map. In this wide-field depiction of six stitched tiles of 15 µm resolution stiffness data, a subset of data points are shown as individual dots for easy of visualisation. OV, optic vesicle; MD, mandibular arch; HY, hyoid arch. (D) Slice view of colour map rendered E9.25 mandibular arch stiffness. (E) Slices at different depths of E9.25 limb bud 3D stiffness map. (F) Time-lapse stiffness map of an E9.25 limb bud.

Figure 3

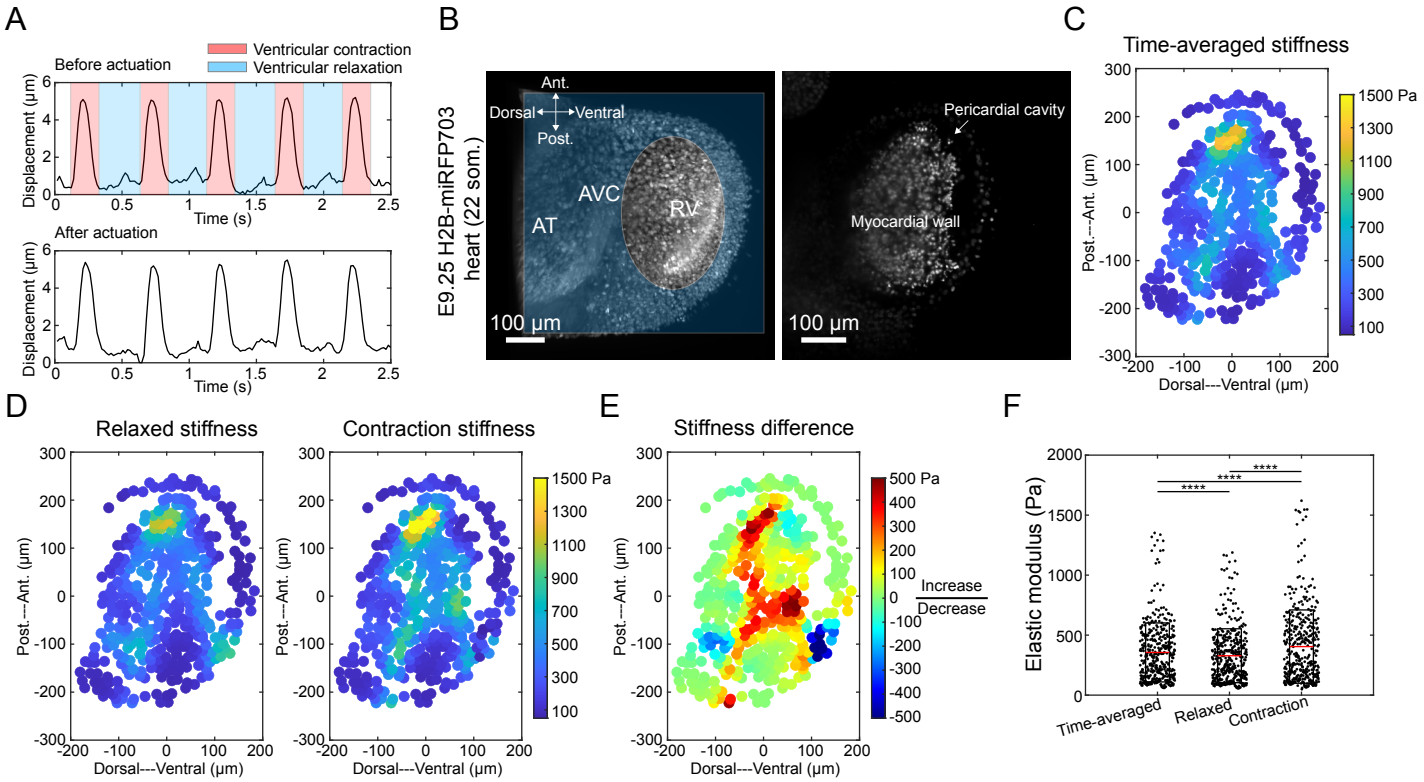

Heart stiffness mapping. (A) Heart nuclear displacements by tracking nuclei before and after actuation showing no changes in beating frequency and rhythm. (B) 3D rendering of an E9.25 H2B-miRFP703 embryonic heart. Right panel showing the focal plane of stiffness mapping. AT, atria; AVC, atrioventricular canal; RV; right ventricle. (C) Time-averaged heart stiffness map. (D) Heart stiffness mapped during ventricular relaxation and decoupled ventricular contraction stiffness map. (E) Heart stiffness difference between ventricular relaxation and contraction. (F) Box plot showing time-averaged, relaxed and contraction-phase heart stiffness (two-tailed paired Student's t-test, ****$P < 0.0001$).

Figure S1

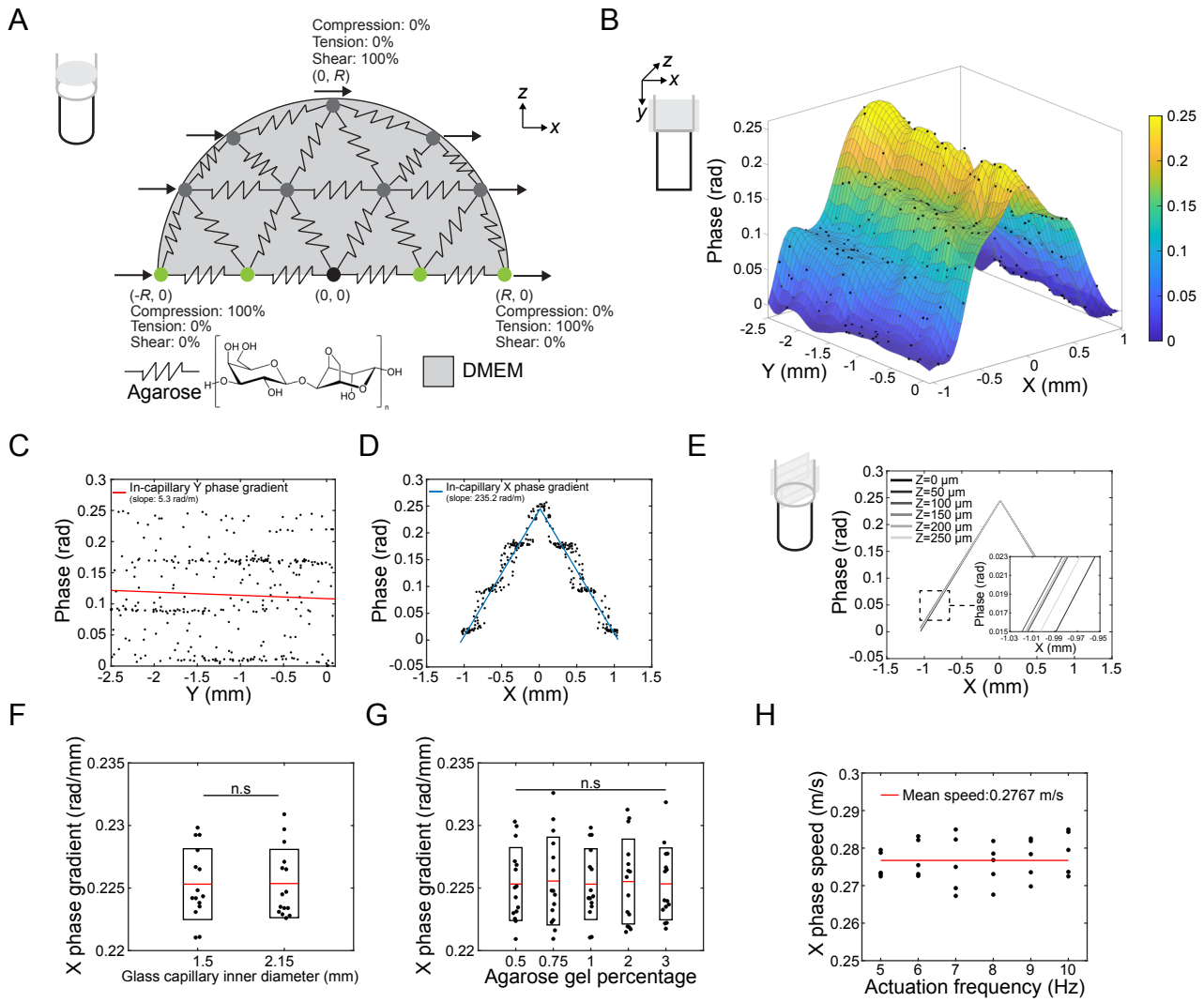

Baseline (X) phase pattern. (A) Schematic depicting the poroelastic agarose gel and boundary conditions at the gel-capillary interface. (B) 3D rendered phase map of 1% agarose gel inside glass capillary under 10 Hz actuation. (C and D) Glass capillary phase along Y axis (C) and X axis (D). (E-G) X phase gradient is independent of the Z location (E), glass capillary diameter (F), and agarose gel percentage (G). (n=3 for each diameter and gel percentage, two-tailed unpaired Student's t-test). n.s, not significant. (H) Constant X phase speed under different actuation frequencies suggesting a non-dispersive X wave.

Figure S2

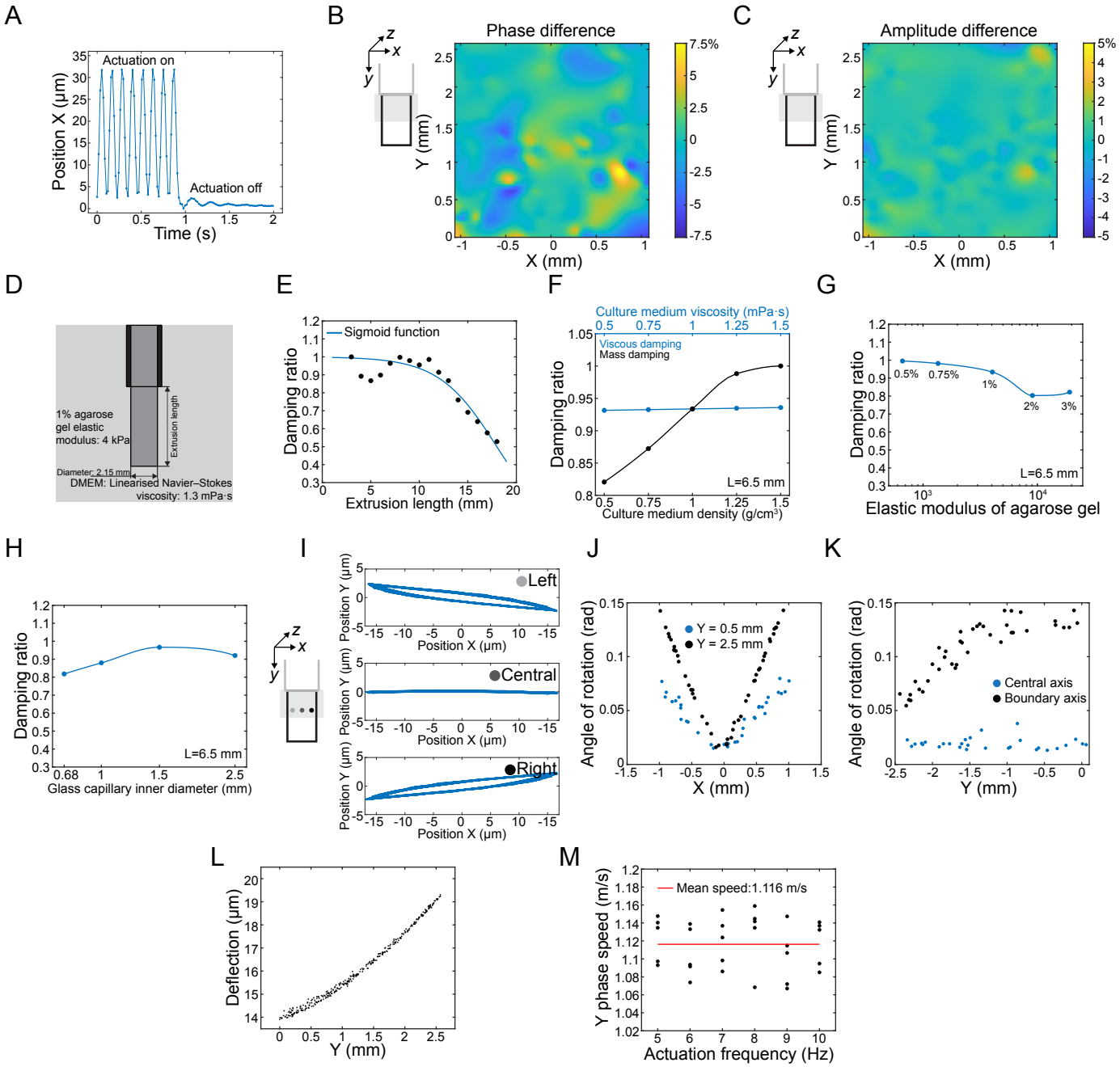

Y phase pattern. (A) Representative position tracking of a fluorescent bead in 1% agarose gel upon 10 Hz actuation. (B and C) 3D rendered phase and amplitude difference submerged in DMEM vs water at 37°C. (D) Fluid-structure interaction simulation model setup. (E) Simulation-predicted damping ratio as a function of the gel extrusion length. (F) Simulation-predicted damping ratio at varying viscosity and culture medium density with an extrusion length of 6.5 mm suggesting predominantly mass damping. (G and H) Simulation -predicted damping ratio at various agarose gel elastic moduli (G) and diameters (H) with an extrusion length of 6.5 mm. (I and J) Angle of rotation along central-boundary axis. (K) Angle of rotation along Y axis. (L) Increased deflection along Y axis. (M) Constant Y phase speed under different actuation frequencies suggesting non-dispersive shear wave propagation along the Y axis.

Figure S3

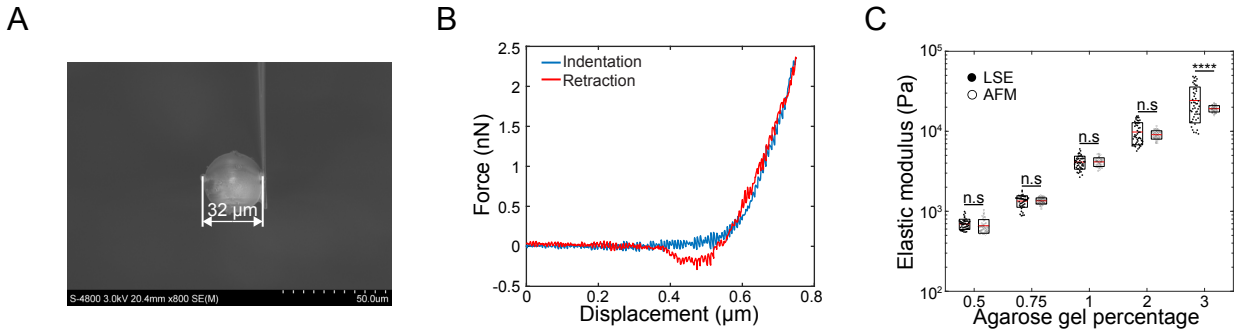

AFM validation. (A) Scanning electron micrograph of an AFM cantilever with a spherical tip of 32 µm diameter. (B) Representative AFM indentation-retraction curve without hysterisis suggesting elastic behaviour of the agarose gel. (C) Comparison of agarose gels at different concentrations with distinct elastic moduli measured by LSE and AFM (n=3 for each gel percentage, two-tailed unpaired Student's t-test, ****$P < 0.0001$). n.s, not significant.

Figure S4

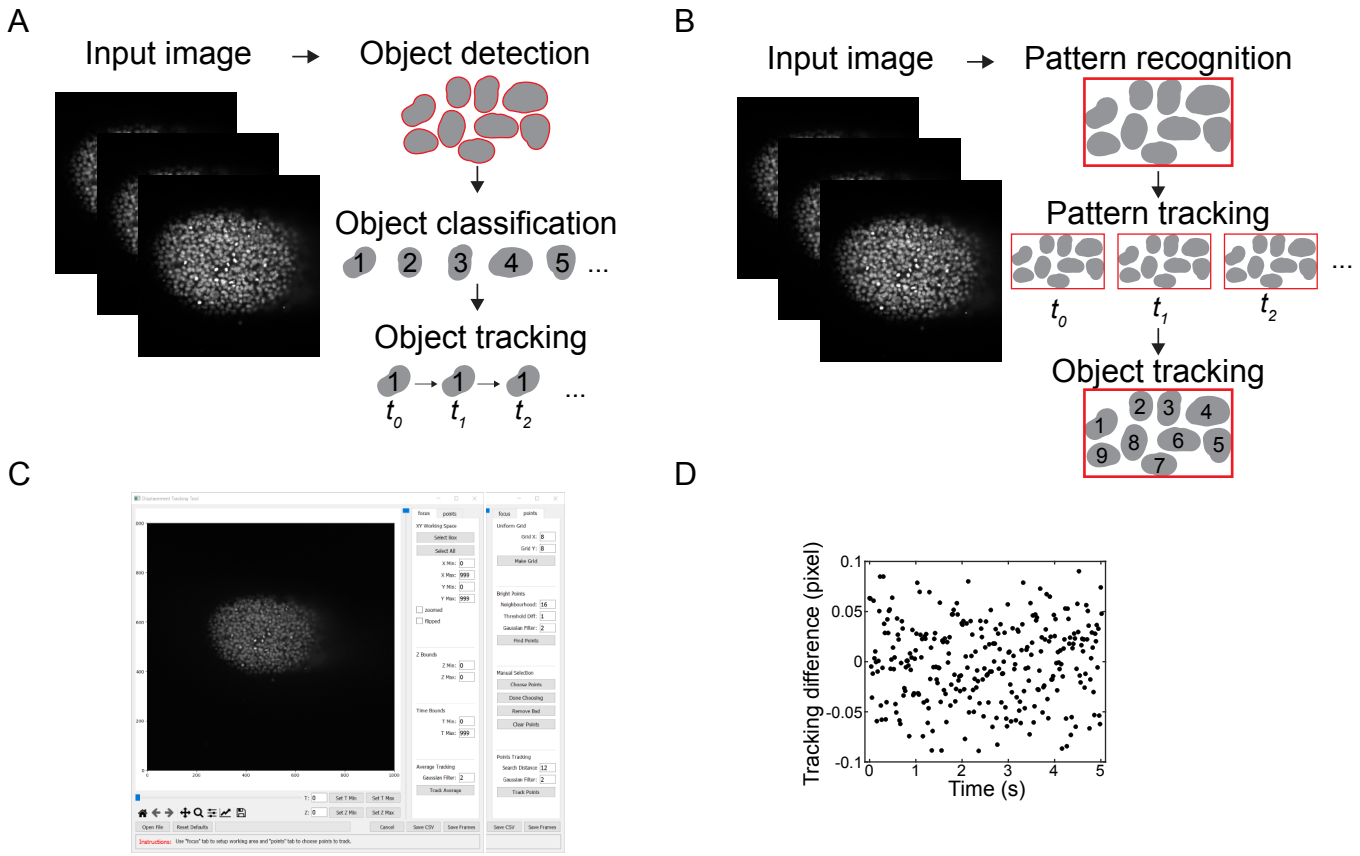

Pattern-guided cell motion tracking program. (A) Schematic describing the autoregressive motion algorithm used in Imaris. (B) Schematic describing the tracking algorithm used in pattern-guided cell motion tracking program. (C) GUI of the pattern-guided cell motion tracking program. Neighbourhood represents the density of the cells. (D) Imaris and PCMT sub-pixel level tracking difference of a fluorescent bead embedded in 1% agarose gel under 10 Hz actuation.

Figure S5

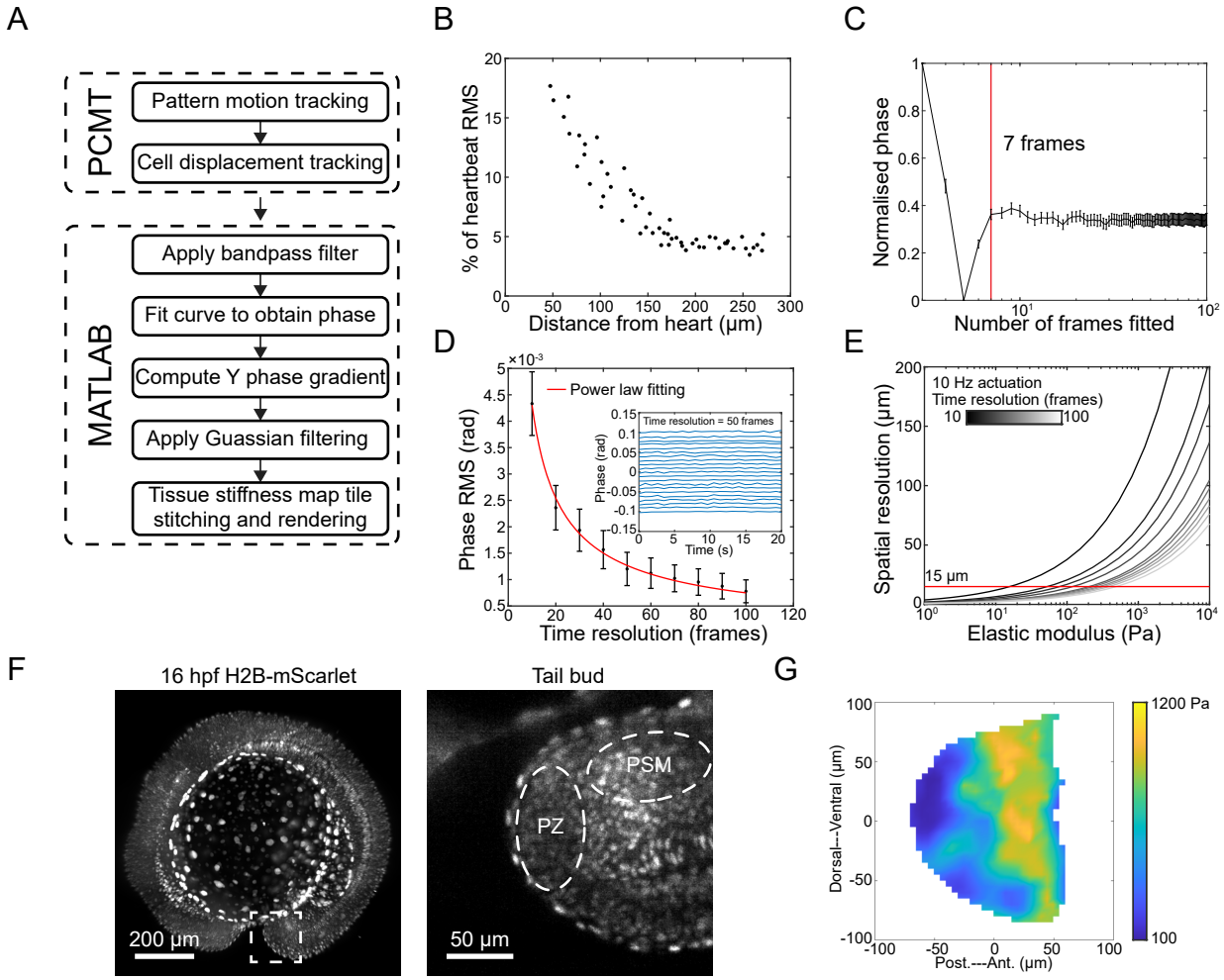

Non-invasive tissue stiffness mapping. (A) Flowchart illustrating LSE analysis pipeline. (B) Heart beat effect decays over distance. (C) LSE time resolution. (D) Phase root mean square (RMS) as a function of time resolution (inset: examples of phase fluctuation over time at 50 frames time resolution). (E) LSE spatial resolution as a function of time resolution, actuation frequency and sample stiffness. (F) 3D rendering of a 16 hpf H2B-mScarlet zebrafish embryo. Right panel showing a zoomed-in view of the tail bud. PZ, progenitor zone; PSM, presomitic mesoderm. (G) Tail bud stiffness map showing an anterior to posterior stiffness gradient.